Systematic model-independent S-matrix analysis of ^{4}He-^{40}Ca elastic scattering in going from anomalous large-angle scattering to near-Coulomb-barrier scattering

V. Yu. Korda,[1,*] A. S. Molev,[1] L. P. Korda,[1,2] and V. F. Klepikov[1]

[1]*Institute of Electrophysics and Radiation Technologies, National Academy of Sciences of Ukraine, 28 Chernyshevsky Street,*
Post Office Box 8812, UA-61002 Kharkov, Ukraine
[2]*NSC Kharkov Institute of Physics and Technology, National Academy of Sciences of Ukraine,*
1 Akademicheskaya Street, UA-61108 Kharkov, Ukraine

Applying the evolutionary model-independent S-matrix approach, we show that a simultaneous correct description of the ^{4}He-^{40}Ca elastic scattering patterns observed in going from anomalous large-angle scattering to near-Coulomb-barrier scattering (NCBS) can be achieved in a unified way using S-matrix moduli and real parts of nuclear phase, which are smooth and monotonic functions of an angular momentum, while quantum deflection functions retain a form characteristic of the nuclear rainbow case. Mechanism of NCBS pattern formation and transformation of the pattern into a pure Coulomb scattering pattern with decreasing energy in the presence of strong nuclear refraction is revealed.

I. INTRODUCTION

To date, the ^{4}He-^{40}Ca elastic scattering differential cross sections at $E \approx 5$–25 MeV/nucleon that show patterns of nuclear rainbow, prerainbow, and anomalous large-angle scattering (ALAS) have been thoroughly investigated both experimentally and theoretically (see, e.g., Refs. [1–7]). These scattering patterns were jointly analyzed using various representations for the optical potential (see, e.g., Refs. [2,7–11]) that generate S-matrix moduli and real parts of nuclear phase having nonmonotonic behavior in the angular momentum space in the cases of prerainbow and ALAS (see, e.g., Refs. [1,5,12,13]). The same quantities obtained within the S-matrix approach of Ref. [12] for the case of ALAS also turned out to be nonmonotonic.

Neither the optical potential, nor the scattering matrix used in theoretical analyses can be experimentally measured and are usually determined using various "physically reasonable" assumptions that depend more or less on the model, since the functions used to model the characteristics under consideration are more or less properly parameterized analytical functions. Thus, the spaces for finding all possible shapes for optical potential and S matrix are substantially reduced, and consequently data analyses performed within such spaces might lead to an incorrect physical interpretation of the data.

That is why it would be highly desirable to use a procedure that could extract the scattering matrix and/or optical potential directly from the experimental data without introducing any bias toward some *a priori* "physically reasonable" model assumptions. The question that this procedure should answer is whether nonmonotonic (e.g., polelike) structures and any other distortions that appear in S-matrix moduli and real

nuclear phases obtained in the most successful approaches are necessary to reproduce the experimental data under study.

The quality of fitting the calculated differential cross section to the experimentally measured one is usually estimated by means of the standard χ^2 magnitude, which is a functional, so its minimization is a variational problem. In Ref. [14] we present a universal evolutionary algorithm that evolves a population of numerical solutions of a variational problem. Our algorithm guarantees a gradual and smooth transformation of the initial population of poorly fitted solutions into a finite population of well fitted ones. The evolved solutions are model-independent, smooth, can have a predefined shape (if necessary), and satisfy the boundary conditions or any other additional physical conditions (if they are imposed).

Applying the evolutionary model-independent S-matrix approach [15] that implements the mentioned algorithm, we have achieved the consistent unified description of all the observed ^{4}He-^{40}Ca elastic scattering pictures at $E \approx 7$–21 MeV/nucleon using conventional smooth monotonic dependencies of S-matrix modulus and the real part of the nuclear phase on the angular momentum in the presence of strong nuclear refraction [16].

With further decrease in the energy of incident particles ($E \lesssim 5$ MeV/nucleon), ALAS picture (with unusual enhancement of regular oscillations at large angles) gradually transforms into a near-Coulomb-barrier scattering (NCBS) picture (without oscillations inherent in ALAS, and with a pronounced influence of the Coulomb interaction of colliding nuclei). Thus far, to our knowledge, neither the smoothly varying global optical potential, nor the single potential family has been found to describe all the variety of scattering pictures (including NCBS picture) observed in the ^{4}He-^{40}Ca elastic scattering at $E < 25$ MeV/nucleon. It is therefore important to extend the unified S-matrix description of the ^{4}He-^{40}Ca elastic scattering achieved in Ref. [16] for $E \approx 7$–21 MeV/nucleon
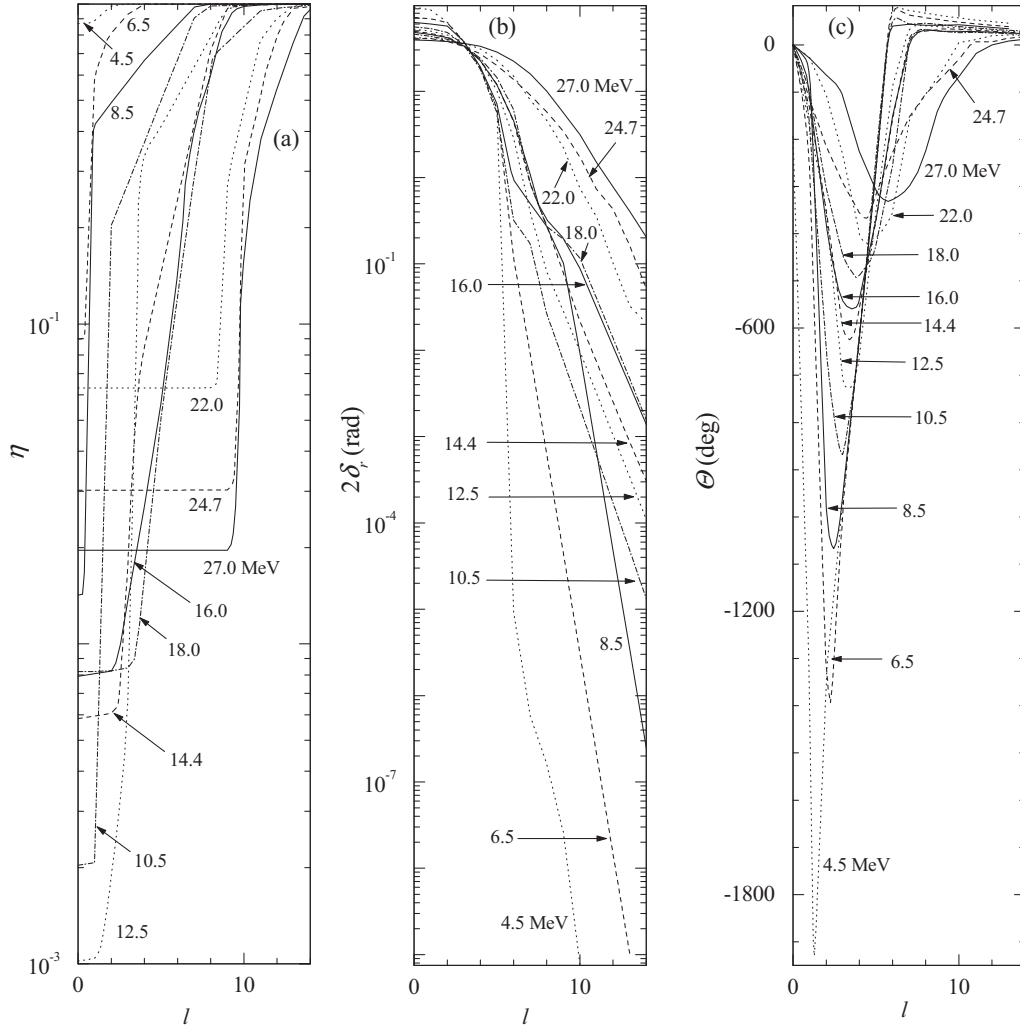
*Corresponding author: kvyu@kipt.kharkov.ua

FIG. 1. (a) Scattering matrix moduli $\eta(l)$, (b) nuclear phases $\delta_r(l)$, and (c) deflection functions $\Theta(l)$ for the ^{4}He-^{40}Ca elastic scattering at $E = 4.5$–27.0 MeV.

to NCBS region in a systematic way using the scattering matrix modulus and the real part of the nuclear phase, which are smooth and monotonic functions of the angular momentum.

II. CALCULATION PROCEDURE

In our approach, the scattering matrix describing the ^{4}He-^{40}Ca elastic scattering has the form $S(l) = S_N(l) \exp[2i\sigma_C(l)]$, where $S_N(l) = \eta(l) \exp[2i\delta_r(l)]$ is the nuclear part, $\sigma_C(l)$ is the Coulomb scattering phase taken to be the quasiclassical phase of point-charge scattering by a uniformly charged sphere with the radius $R_C = 1.3 \times 40^{1/3}$ (see, e.g., Ref. [17]) at above-Coulomb-barrier energies and the ordinary Coulomb phase for scattering of two point charges at lower energies, $\eta(l) = \exp[-2\delta_a(l)]$ is the scattering matrix modulus, $\delta_r(l)$ is the nuclear refraction phase (real part of the nuclear phase), and $\delta_a(l)$ is the nuclear absorption phase (imaginary part of the nuclear phase). Calculations are performed using the expansion of the scattering amplitude into a series

of Legendre polynomials. The elastic scattering differential cross section equals the squared modulus of this amplitude. The quality of fitting the calculated differential cross section to the experimentally measured one is estimated using the standard χ^2 magnitude per datum. The experimental errors are assumed to be equally weighted (10% error bars) (e.g., Refs. [4,12,16,18]).

Our evolutionary model-independent S-matrix approach [14–16] operates on a population of N individuals. Each individual is an S matrix presented as a pair of real-valued l_{max}-dimensional vectors $[\delta_a(l), \delta_r(l)]$, $l = 0, 1, ..., l_{max} - 1$. Fitness of each individual reflects the quality of data fitting provided by the individual's S matrix. Using the mutation operation, the algorithm evolves the initial population of poorly fitted individuals to the final population of the well-fitted ones.

Every iteration, the so-called generation, of our procedure contains the following steps.

(1) Generating the initial population of N individuals. For each individual, vectors $\delta_{a,r}(l)$ are set using a physically

TABLE I. Energy evolution of the values of the nuclear transparency $\eta(0)$, the intensity of nuclear refraction $2\delta_r(0)$, the nuclear rainbow angle θ_R, the total reaction cross section σ_R^t, and the χ^2/N_p magnitude for the calculated cross sections.

E (MeV)	$\eta(0)$	$2\delta_r(0)$ (rad)	θ_R (deg)	σ_R^t (mb)	χ^2/N_p
27.0	1.962×10^{-2}	39.216	332	1269	3.6
24.7	3.025×10^{-2}	41.311	367	1194	3.7
22.0	6.303×10^{-2}	42.145	420	1163	3.8
18.0	8.191×10^{-3}	45.717	494	1008	3.7
16.0	7.922×10^{-3}	48.040	559	968	3.7
14.4	5.838×10^{-3}	49.414	625	963	3.8
12.5	1.017×10^{-3}	52.383	727	954	3.6
10.5	2.031×10^{-3}	55.524	868	813	1.6
8.5	1.421×10^{-2}	62.586	1068	596	0.4
6.5	8.974×10^{-2}	71.694	1393	172	0.3
4.5	8.694×10^{-1}	94.050	1930	45	0.005

justified function:

$$2\delta_i(l) = g_i \ f(l,l_i,d_i),$$

$$f(l,l_i,d_i) = \left[1 + \exp\left(\frac{l - l_i}{d_i} \right) \right]^{-1}, \qquad (1)$$

$$i = a, r.$$

Parameters g_i, l_i, and d_i are positive and are chosen for each individual at random within certain intervals wide enough to obtain substantially different shapes of the phases.

(2) Evaluating fitness of each individual in the population. The fitness function in our approach consists of two parts. The first one is associated with the quality of shapes of $\delta_{a,r}(l)$, and the second one accounts for the quality of fitting of the experimental data.

Shapes of $\delta_{a,r}(l)$ must meet the following requirements:

(i) Functions $\delta_{a,r}(l)$ must be descending.
(ii) The first derivatives of $\delta_{a,r}(l)$ must have only one minimum and no maxima.
(iii) The second derivatives of $\delta_{a,r}(l)$ are allowed to have one deepest minimum, one highest maximum, and an arbitrary number of local minima and maxima that do not substantially influence the shapes of phases.
(iv) The third derivative of $\delta_r(l)$ is allowed to have two deepest minima, one highest maximum, and an arbitrary number of local minima and maxima that do not substantially influence the shape of the real nuclear phase.
(v) Logarithmic derivatives of $\delta_{a,r}(l)$ should be descending in the phase tail region.

The individual for which at least one of these requirements is violated is excluded from the population.

If we remove all the mentioned constraints, we get a better fit, but let the nonmonotonic structures appear in $\eta(l)$ and $\delta_r(l)$. However, the nonmonotonic structures arising in $\eta(l)$ and $\delta_r(l)$ in this case are quite different from run to run of the fitting procedure and from structures obtained within the optical model calculations (e.g., Refs. [1,13,19]) and other S-matrix approaches (e.g., Ref. [12]). Obviously, if and only if the same nonmonotonic structures appear repeatedly in the scattering matrix modulus and/or the real nuclear phase along with the substantial improvement in the quality of fit, one should admit that the existence of these structures is physically motivated and the search for their physical interpretation is justified.

(3) Letting each individual in the population produce $M \gg 1$ offspring. Replication is performed according to the transformation:

$$\log[\delta_i'(l)] = \log[\delta_i(l)] + A_i N_i(0,1) D(l,l_{m,i},d_{m,i}),$$
$$i = a, r, \qquad (2)$$

where $\delta_i(l)$ and $\delta_i'(l)$ are the parent's and the offspring's S-matrix phases, respectively, $A_i > 0$ is the mutation amplitude, $A_i \in [A_{\min}, A_{\max}]$, $N_i(0,1)$ denotes a normally distributed one-dimensional random number with mean zero and one standard deviation, $D(l,l_{m,i},d_{m,i})$ is the mutation diffusing function, $l_{m,i}$ stands for the mutation point chosen randomly, $l_{m,i} \in [0,l_{\max} - 1]$, and $d_{m,i} > 0$ is the value characterizing the diffuseness of the mutation point, $d_{m,i} \in [d_{\min}, d_{\max}]$. The mutation diffusing function has the form

$$D(l, \ l_{m,i}, \ d_{m,i}) = \exp\left[-\frac{(l - l_{m,i})^2}{d_{m,i}^2} \right]. \qquad (3)$$

During the replication of the parent, the values of mutation amplitude and diffuseness are tuned within the specified intervals as follows:

$$A_i' = A_i \exp\left[L N_i(0,1) \right], \qquad (4)$$

$$d_{m,i}' = d_{m,i} \exp\left[L N_i(0,1) \right], \qquad (5)$$

where A_i and $d_{m,i}$ are the values of mutation amplitude and diffuseness of the parent, while A_i' and $d_{m,i}'$ are the same values of the offspring, respectively, L is the learning parameter that controls the speed of tuning. The lengths of the intervals $[A_{\min}, A_{\max}]$ and $[d_{\min}, d_{\max}]$, having large values at the beginning of the procedure, smoothly decrease during the run and acquire small values at the end. This tactic provides for both removal of the features of primary parametrization (1) from the individual's $S(l)$ and fine tuning of details of $S(l)$.

(4) Evaluating fitness values of all offspring. Sort the offspring in descending order according to their fitness. Select N best offspring to form the new population.

(5) Going to step 3 or stop if the best fitness in the population is sufficiently high (the χ^2 value is small enough).

Evolutionary algorithms make up, generally, the global optimization technique that, however, cannot guarantee that the optimum found is the global one. Therefore, it is necessary
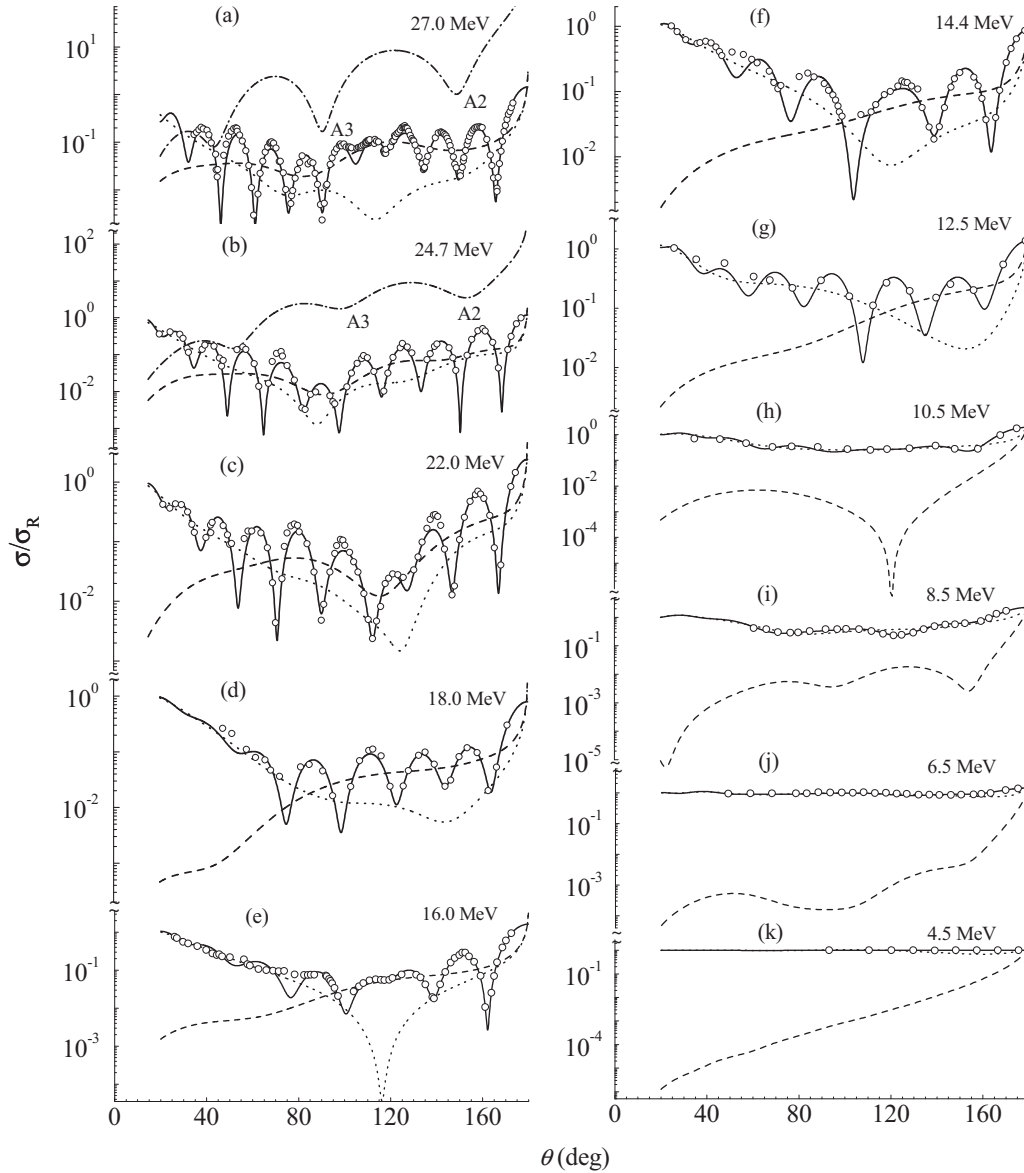
FIG. 2. (a)–(k) Elastic scattering differential cross sections (ratio to Rutherford) for the system ^{4}He + ^{40}Ca at $E = 4.5$–27.0 MeV (solid curves), their farside (dashed curves) and nearside (dotted curves) components, and farside cross-section components calculated without absorption in the scattering matrix [dash-dotted curves in Figs. 2(a) and 2(b)]. $A2$ and $A3$ denote the Airy minima of second and third orders. The data are from Refs. [3,6,24–29] .

to run the procedure several times. Besides, there is no way to know in advance what the minimum value of the χ^2 magnitude will be. Thus, it is instructive to follow the dynamics of the best, worst, and mean fitness values and the root-mean-square deviation from the mean fitness in the population during those several runs of the procedure in order to localize the region of the lowest χ^2 values.

Near the Coulomb barrier, the role of couplings between different reaction channels and their contribution to the elastic scattering may increase (see, e.g., Refs. [20,21]), but we suppose that such processes, if present, are reflected in the behavior of the scattering matrix extracted from the data.

More detailed analysis of complicated structures inherent in the elastic scattering cross sections under discussion can be

performed with the use of the nearside-farside decomposition [22]. To detect the Airy structures, we use both the farside component and the farside component calculated without absorption in the scattering matrix [$\eta(l) = 1$ for all l].

III. RESULTS OF CALCULATIONS AND THEIR DISCUSSION

Searching for the S-matrix representations for the ^{4}He-^{40}Ca elastic scattering at $E = 4.5$–27.0 MeV, we have taken into account the energy systematics built in Ref. [16] for angular positions of the Airy minima and the Fraunhofer crossover point, the nuclear rainbow angle θ_R that corresponds to the minimum of deflection function $\Theta(l) = 2d[\delta_r(l) + \sigma_C(l)]/dl$,
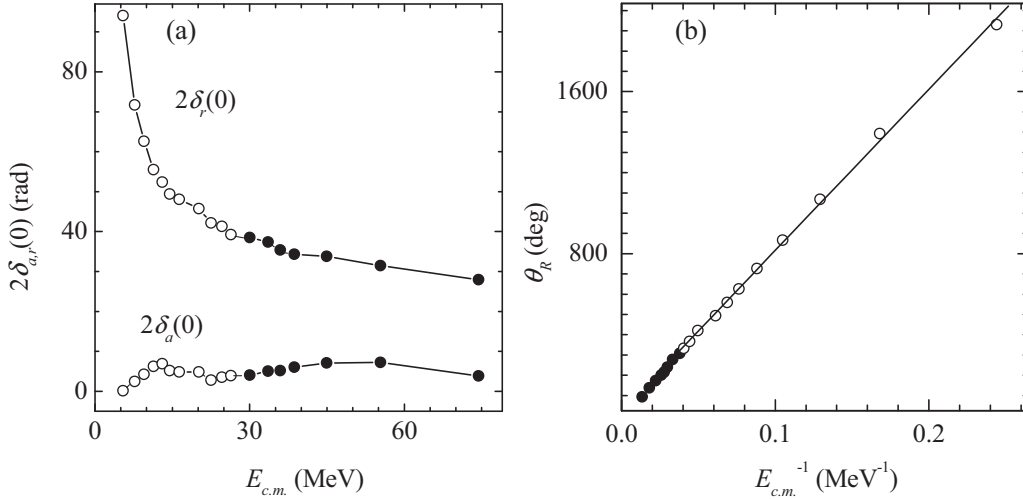
FIG. 3. (a) Evolution with center-of-mass energy of the intensities of nuclear refraction $2\delta_r(0)$ and nuclear absorption $2\delta_a(0)$ for the system $^4\text{He} + {}^{40}\text{Ca}$ (open circles). Solid curves are only to guide the eye. (b) Evolution with reciprocal center-of-mass energy of the nuclear rainbow angle θ_R (open circles). Straight line shows results of fitting to the data indicated as circles. The results of calculations performed in Ref. [16] are shown as solid circles.

the nuclear transparency $\eta(0)$, the intensity of nuclear refraction $2\delta_r(0)$, the strong absorption angular momentum, and the total reaction cross section σ_R^t.

Figures 1(a), 1(b) and the Supplemental Material [23] show scattering matrices for the ^4He-^{40}Ca elastic scattering, found using our approach. Figure 1(c) presents quantum deflection functions. In each of the cases studied, from ALAS to NCBS, data in the whole angular range under consideration are correctly described by the differential cross section (Fig. 2) calculated with the obtained smooth monotonic representations for the scattering matrix modulus and the nuclear phase (Fig. 1). The energy evolution of the values of $\eta(0)$, $2\delta_r(0)$, θ_R, σ_R^t, and χ^2/N_p (N_p is the number of experimental points) for the calculated cross sections is presented in Table I.

At $E = 1$–21 MeV/nucleon, evolution with center-of-mass energy of the values of intensity of the nuclear refraction $2\delta_r(0)$ and nuclear absorption $2\delta_a(0)$ is presented in Fig. 3(a), and dependence of the nuclear rainbow angle θ_R on the reciprocal center-of-mass energy is shown in Fig. 3(b). Note a systematic decrease of $2\delta_r(0)$ and a smooth behavior of $2\delta_a(0)$ with increasing energy: the quantity $2\delta_a(0)$ increases in NCBS region, decreases in the region where NCBS picture transforms into ALAS one, increases in ALAS region, and decreases in the region of nuclear rainbow scattering.

The quantum deflection function $\Theta(l)$ in the region $E = 1$–7 MeV/nucleon is typical of the nuclear rainbow case. With decreasing energy, its form becomes narrower in the region of negative values but remains mostly symmetric in the vicinity of a minimum [Fig. 1(c)]. The nuclear rainbow angle θ_R obeys the law of the reciprocal center-of-mass energy dependence [Fig. 3(b)].

The Fraunhofer crossover point for $E = 16.0$, 14.4, and 12.5 MeV is situated at $\theta \approx 92°$, 98°, and 118°, respectively, and consequently the calculated differential cross sections seem "too oscillatory" with respect to the data around 80° at $E = 16.0$ and 14.4 MeV, and in a wide angular range (up to 140°) at $E = 12.5$ MeV. This does not noticeably affect the

values of the χ^2 magnitude because, for the given experimental errors, the data for $\theta > 80°$ at $E = 16.0$ and 14.4 MeV and the limited data available at $E = 12.5$ MeV are well described by the calculated cross sections.

The measured differential cross sections for the ^4He-^{40}Ca elastic scattering at $E = 27.0$ MeV [Fig. 2(a)] and $E = 24.7$ MeV [Fig. 2(b)] have well pronounced minima at $\theta \approx 90°$ and $\theta \approx 100°$, respectively. These minima are mainly reproduced by the farside components [dashed curves in Figs. 2(a) and 2(b)]. If we take into account the systematics for the positions of the second order Airy minima $A2$ build in Ref. [16], they could be the third order Airy minima $A3$ that exist in the farside components calculated without absorption in the scattering matrix [dash-dotted curves in Figs. 2(a) and 2(b)]. Unfortunately, the Airy minima $A3$ do not appear in the calculated cross sections because they are obscured by the farside-nearside interference, so that the existing minima have the interference nature. Thus, we have not identified the Airy minima in the ^4He-^{40}Ca elastic scattering cross sections at $E \lesssim 7$ MeV/nucleon.

IV. ANALYSIS OF FORMATION OF NCBS PATTERN

NCBS picture is characterized by strong damping of oscillations of the measured differential cross section and gradual transformation of the latter into a pure Coulomb scattering cross section with decreasing energy [Figs. 2(h)–2(k)].

In our analysis, damping of oscillations of the calculated differential cross sections is associated with the absence of the Fraunhofer crossover point and the predominance of the nearside scattering [Figs. 2(h)–2(k)]. We note that a drastic transformation of the calculated differential cross section occurs between $E = 12.5$ MeV and $E = 10.5$ MeV. Let us indicate the particular partial waves responsible for this transformation. With this aim in view, in our calculations for $E = 12.5$ MeV we manually replace the original experimental
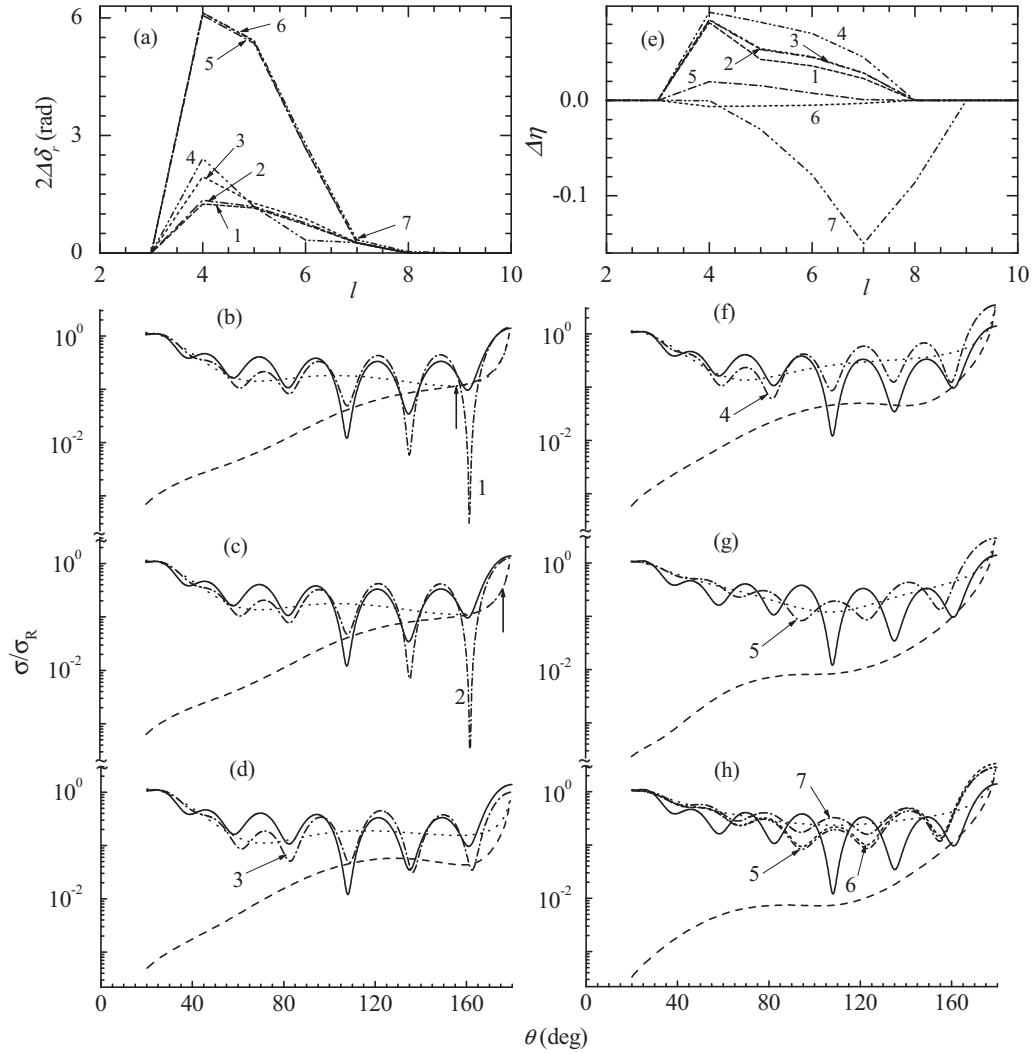
FIG. 4. Analysis of the formation of NCBS pattern for the system ^{4}He + ^{40}Ca at $E = 12.5$ MeV. (a) [(e)] Differences $\Delta\delta_r(l) [\Delta\eta(l)]$ between the nuclear phase (the scattering matrix modulus) extracted from the data at $E = 12.5$ MeV (same as in Fig. 1) and the result of its evolution caused by the data at $E = 10.5$ MeV. The angular momentum regions where our evolutionary approach has changed the scattering matrix are $\Delta l = 4$–7 (curves 1–6) and $\Delta l = 4$–8 (curve 7). (b)–(d) and (f)–(h) Elastic scattering differential cross sections (ratio to Rutherford). Solid curves are the same as in Fig. 2(g). The curves marked with numbers are calculated using the scattering matrices shown (in the form of differences) in Figs. 4(a) and 4(e) (numbers of curves correspond). Dashed and dotted curves in Figs. 4(b)–4(d), 4(f), and 4(g) present the farside and nearside components of the cross sections marked as 1–5. Dashed and dotted curves in Fig. 4(h) show the farside and nearside components of the cross section marked as 7. Vertical arrows in Figs. 4(b) and 4(c) mark the positions of the Fraunhofer crossover point.

data by the data taken at $E = 10.5$ MeV. Then we continue our evolutionary calculations using these data, but starting with the scattering matrix extracted from the original data at $E = 12.5$ MeV, and allowing the mutation operation to change the scattering matrix in some angular momentum region Δl. We are looking for the narrowest possible Δl for which the evolved scattering matrix generates differential cross section that has NCBS features. In order to analyze in detail the mechanism of NCBS pattern formation, evolving the scattering matrix for the given Δl, we store all the intermediate information, generation after generation, about the fittest scattering matrix and the differential cross section calculated with this scattering matrix, as well as the farside and nearside cross-section components.

Figure 4 presents some of our results obtained in this way. Figure 4(a) [4(e)] shows the differences $\Delta\delta_r(l) [\Delta\eta(l)]$ between the nuclear phase (the scattering matrix modulus) extracted from the data at $E = 12.5$ MeV (same as in Fig. 1) and the result of its evolution caused by the data at $E = 10.5$ MeV. The angular momentum regions where our evolutionary approach has changed the scattering matrix are $\Delta l = 4$–7 (curves 1–6) and $\Delta l = 4$–8 (curve 7). Figures 4(b)–4(d) and 4(f)– 4(h) show the elastic scattering differential cross sections calculated using the evolved scattering matrices. Solid curves are the same as in Fig. 2(g). The curves marked with numbers are calculated using the scattering matrices shown (in the form of differences) in Figs. 4(a) and 4(e) (numbers of curves correspond). Dashed and dotted curves in Figs. 4(b)–4(d), 4(f)
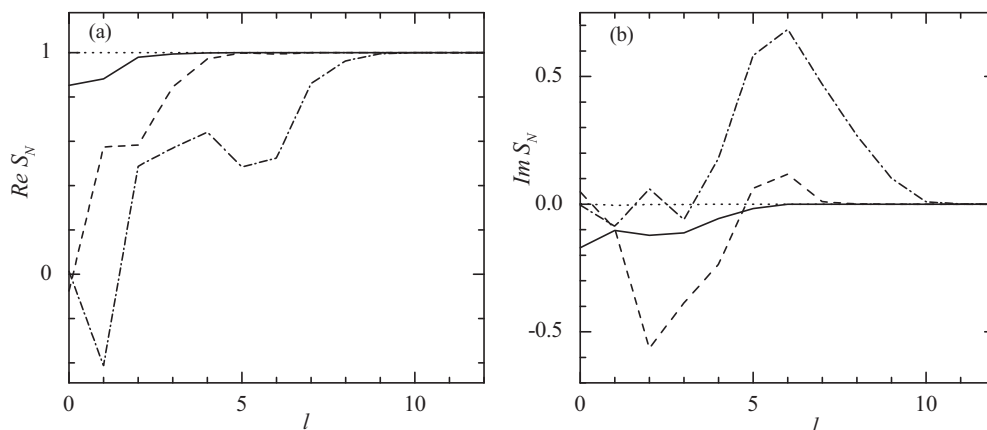
FIG. 5. Analysis of the formation of a pure Coulomb scattering pattern in the presence of strong nuclear refraction for the system ^{4}He + ^{40}Ca. (a) and (b) Real Re$S_N(l)$ and imaginary Im$S_N(l)$ parts of the nuclear scattering matrix $S_N(l)$. Solid, dashed, and dash-dotted curves are the results for $E = 4.5$, 6.5, and 8.5 MeV, respectively (same as in Fig. 1). Dotted curves show the results of the evolution of the nuclear scattering matrix extracted from the data at $E = 4.5$ MeV (solid curves) caused by the artificial data that is a pure Coulomb scattering cross section at the same energy.

and 4(g) present the farside and nearside components of the cross sections marked as 1–5. Dashed and dotted curves in Fig. 4(h) show the farside and nearside components of the cross section marked as 7. Vertical arrows in Figs. 4(b) and 4(c) mark the positions of the Fraunhofer crossover point.

We see that gradual decrease in nuclear refraction and nuclear transparency at $\Delta l = 4$–7 leads to the fact that the Fraunhofer crossover point moves toward $\theta = 180°$ [Figs. 4(b) and 4(c)] and disappears [Fig. 4(d)], and then the farside and nearside components move away from each other [Fig. 4(f)]. In all these cases, the calculated differential cross sections oscillate in phase with the differential cross section obtained for $E = 12.5$ MeV. A further decrease in nuclear refraction and a gradual increase in nuclear transparency at $\Delta l = 4$–7 lead to the fact that the farside and nearside components are transformed in such a way that the calculated differential cross sections begin to oscillate in phase with the differential cross section for $E = 10.5$ MeV [Figs. 4(g) and 4(h), curves 5 and 6]. If at this point we extend the region of angular momenta where our evolutionary approach changes the scattering matrix up to $\Delta l = 4$–8 the nuclear refraction remains almost the same but the nuclear transparency substantially increases, which leads to the increase in the dominant nearside component at midangles [Fig. 4(h), curve 7]. This study reveals the special role of several surface partial waves in the formation of NCBS pattern.

In our analysis, gradual transformation of the calculated differential cross section into a pure Coulomb scattering cross section with decreasing energy is associated with gradual transformation of the real Re$S_N(l)$ and imaginary Im$S_N(l)$ parts of the nuclear scattering matrix $S_N(l)$ into unity and zero, respectively (Fig. 5). Solid, dashed, and dash-dotted curves represent the results for $E = 4.5$, 6.5, and 8.5 MeV, respectively (same as in Fig. 1). Dotted curves show the result of the evolution of the nuclear scattering matrix extracted from the data at $E = 4.5$ MeV (solid curves) caused by the artificial data that is a pure Coulomb scattering cross section at the same energy. In this case, the evolved values of the scattering matrix modulus $\eta(l)$ and the nuclear phase $2\delta_r(l)$ are very close to unity

and multiples of 2π (for all l), respectively. Thus, the transition to a pure Coulomb scattering picture in the presence of strong nuclear refraction becomes possible due to strong suppression of the nuclear absorption and the closeness of the values of the nuclear refraction phase $2\delta_r(l)$ to multiples of 2π for all l.

V. CONCLUSION

Applying the evolutionary model-independent S-matrix approach, we have shown that a simultaneous correct description of the whole variety of the scattering pictures observed in the system ^{4}He+^{40}Ca at $E = 1$–21 MeV/nucleon (including pictures of the nuclear rainbow, prerainbow, ALAS, and NCBS) can be achieved in a unified way using S-matrix moduli and real nuclear phases, which are smooth and monotonic functions of the angular momentum. The quantum deflection functions have a form characteristic of the nuclear rainbow case and are mostly symmetric in the vicinity of a minimum. The scattering matrix and the quantum deflection function for the system ^{4}He + ^{40}Ca at $E = 4.5$–82.0 MeV show smooth physically motivated variations with the projectile energy. The nuclear rainbow angle obeys the law of the reciprocal center-of-mass energy dependence. Systematic description of the ^{4}He-^{40}Ca elastic scattering at $E = 1$–21 MeV/nucleon is achieved in the presence of strong nuclear refraction and is in line with the rainbow interpretation of the data.

No Airy minima higher than the second order have been identified in the ^{4}He-^{40}Ca elastic scattering cross sections.

We have revealed that the formation of NCBS picture is associated with a substantial suppression of nuclear refraction and nuclear absorption for several surface partial waves. The transition to a pure Coulomb scattering picture in the presence of strong nuclear refraction becomes possible due to strong suppression of the nuclear absorption and the closeness of the values of the nuclear refraction phase $2\delta_r(l)$ to multiples of 2π in the whole region of angular momenta.

A unified study of the pictures of the nuclear rainbow and prerainbow scattering, ALAS and NCBS in the system ^{4}He +

^{40}Ca, performed within the evolutionary model-independent S-matrix approach, has helped us to understand the interaction between the colliding nuclei systematically.

[1] F. Michel, S. Ohkubo, and G. Reidemeister, Prog. Theor. Phys. Suppl. **132**, 7 (1998).

[2] Th. Delbar, Gh. Gregoire, G. Paic, R. Ceuleneer, F. Michel, R. Vanderpoorten, A. Budzanowski, H. Dabrowski, L. Freindl, K. Grotowski, S. Micek, R. Planeta, A. Strzalkowski, and K. A. Eberhard, Phys. Rev. C **18**, 1237 (1978).

[3] H. P. Gubler, U. Kiebele, H. O. Meyer, G. R. Plattner, and I. Sick, Phys. Lett. B **74**, 202 (1978); Nucl. Phys. A **351**, 29 (1981).

[4] H. Löhner, H. Eickhoff, D. Frekers, G. Gaul, K. Poppensieker, R. Santo, A. G. Drentje, and L. W. Put, Z. Phys. A **286**, 99 (1978).

[5] K. W. McVoy, H. M. Khalil, M. M. Shalaby, and G. R. Satchler, Nucl. Phys. A **455**, 118 (1986).

[6] G. Gaul, H. Lü decke, R. Santo, H. Schmeing, and R. Stock, Nucl. Phys. A **137**, 177 (1969).

[7] S. Ohkubo, Phys. Rev. C **38**, 2377 (1988).

[8] F. Michel and R. Vanderpoorten, Phys. Lett. B **82**, 183 (1979).

[9] M. N. A. Abdullah, A. B. Idris, A. S. B. Tariq, M. S. Islam, S. K. Das, M. A. Uddin, A. S. Mondal, A. K. Basak, I. Reichstein, H. M. Sen Gupta, and F. B. Malik, Nucl. Phys. A **760**, 40 (2005).

[10] T. Furumoto and Y. Sakuragi, Phys. Rev. C **74**, 034606 (2006).

[11] A. H. Al-Ghamdi, A. A. Ibraheem, and M. El-Azab Farid, Int. J. Mod. Phys. E **24**, 1550003 (2015).

[12] M. C. Mermaz, Phys. Rev. C **27**, 2019 (1983).

[13] F. Michel and G. Reidemeister, Phys. Rev. C **29**, 1928 (1984).

[14] V. Yu. Korda, S. V. Berezovsky, A. S. Molev, V. F. Klepikov, and L. P. Korda, Int. J. Mod. Phys. C **24**, 1350009 (2013).

[15] V. Yu. Korda, A. S. Molev, and L. P. Korda, Phys. Rev. C **72**, 014611 (2005).

[16] V. Yu. Korda, A. S. Molev, V. F. Klepikov, and L. P. Korda, Phys. Rev. C **91**, 024619 (2015).

[17] Yu. A. Berezhnoy and V. V. Pilipenko, Mod. Phys. Lett. A **10**, 2305 (1995).

[18] V. Yu. Korda, A. S. Molev, L. P. Korda, and V. F. Klepikov, Phys. Rev. C **79**, 024601 (2009).

[19] I. Jamir, E. F. P. Lyngdoh, and C. S. Shastry, Phys. Rev. C **57**, 1000 (1998).

[20] G. R. Satchler, Phys. Rep. **199**, 147 (1991).

[21] A. Pakou, N. Alamanos, A. Lagoyannis, A. Gillibert, E. C. Pollacco, P. A. Assimakopoulos, G. Doukelis, K. G. Ioannides, D. Karadimos, D. Karamanis, M. Kokkoris, E. Kossionides, N. G. Nicolis, C. Papachristodoulou, N. Patronis, G. Perdikakis, and D. Pierroutsakou, Phys. Lett. B **556**, 21 (2003).

[22] R. C. Fuller, Phys. Rev. C **12**, 1561 (1975).

[23] See Supplemental Material at http://link.aps.org/supplemental/10.1103/PhysRevC.97.034606 for the scattering matrices for the ^{4}He-^{40}Ca elastic scattering at $E = 4.5$–27.0 MeV, found using our approach.

[24] A. Budzanowski, K. Grotowski, S. Micek, H. Niewodniczański, J. Śliz, A. Strzał kowski, and H. Wojciechowski, Phys. Lett. **11**, 74 (1964).

[25] M. Makowska-Rzeszutko, A. Dudek, and A. Drzymała, Acta Phys. Pol. B **2**, 771 (1971).

[26] C. P. Robinson, J. P. Aldridge, J. John, and R. H. Davis, Phys. Rev. **171**, 1241 (1968).

[27] J. John, C. P. Robinson, J. P. Aldridge, and R. H. Davis, Phys. Rev. **177**, 1755 (1969).

[28] J. P. F. Sellschop, A. Zucchiatti, L. Mirman, M. Z. I. Gering, and E. Di Salvo, J. Phys. G **13**, 1129 (1987).

[29] D. Frekers, R. Santo, and K. Langanke, Nucl. Phys. A **394**, 189 (1983).